Energetics of Bacterial Photosynthesis

David N. LeBard[†,‡] **and Dmitry V. Matyushov**[*,†]

Center for Biological Physics, Arizona State University, P.O. Box 871604, Tempe, Arizona 85287-1604

Received: May 18, 2009; Revised Manuscript Received: July 27, 2009

We report the results of extensive numerical simulations and theoretical calculations of electronic transitions in the reaction center of *Rhodobacter sphaeroides* photosynthetic bacterium. The energetics and kinetics of five electronic transitions related to the kinetic scheme of primary charge separation have been analyzed and compared to experimental observations. Nonergodic formulation of the reaction kinetics is required for the calculation of the rates due to a severe breakdown of the system ergodicity on the time scale of primary charge separation, with the consequent inapplicability of the standard canonical prescription to calculate the activation barrier. Common to all reactions studied is a significant excess of the charge-transfer reorganization energy from the width of the energy gap fluctuations over that from the Stokes shift of the transition. This property of the hydrated proteins, breaking the linear response of the thermal bath, allows the reaction center to significantly reduce the reaction free energy of near-activationless electron hops and thus raise the overall energetic efficiency of the biological charge-transfer chain. The increase of the rate of primary charge separation with cooling is explained in terms of the temperature variation of induction solvation, which dominates the average donor−acceptor energy gap for all electronic transitions in the reaction center. It is also suggested that the experimentally observed break in the Arrhenius slope of the primary recombination rate, occurring near the temperature of the dynamical transition in proteins, can be traced back to a significant drop of the solvent reorganization energy close to that temperature.

Introduction

Fast and unidirectional primary charge separation occurs in reaction centers of photosynthetic bacteria upon absorption of a visible photon from the bacterial antenna system. This process proceeds as a sequence of two electron hops taking together about 3−4 ps in the reaction center of the purple bacterium *Rb. sphaeroides*.[1,2] This is followed, within $\simeq$200 ps, by the next electron hop to the quinone cofactor. Electron transport proceeds with an exceptionally high quantum yield close to unity, thus raising the following questions: how is it achieved in the protein matrix of the reaction center, and what are the energetic transformations in the process? Answering these questions, which we will dub as the energetics of primary charge separation, is critical for the modeling of the entire photosynthetic apparatus. Even more important, one wants to understand the generic mechanisms, selected by evolution, of charge transport in bacteria. This knowledge will help to formulate fundamental principles of efficient transformation of light energy into the energy of the charge-separated state in molecular systems. The purpose of this paper is to study, by means of numerical molecular dynamics (MD) simulations, the energetic balance of bacterial primary charge separation and recombination.

For a radiationless transition, Fermi's golden rule requires the resonance of the donor, E_D, and acceptor, E_A, energy levels. The transition probability is then proportional to the density of states, $\propto \langle \delta(E_A - E_D) \rangle$. The average of the delta function here is over the thermal nuclear fluctuations in the system. When Gaussian approximation is used to describe these fluctuations, the density of states (the Franck−Condon factor) is given in terms of two parameters, the average separation of the donor and acceptor energy levels, $\langle \Delta E \rangle = \langle E_A - E_D \rangle$, and the Gaussian width σ. The Marcus formulation of the electron-transfer kinetics[3] allows access to both parameters through the electron-transfer reorganization energy λ. Specifically, the average energy gap is obtained by combining λ with the reaction Gibbs energy ΔG_0, $\langle \Delta E \rangle = \Delta G_0 + \lambda$, while the Gaussian width is obtained by multiplying λ with temperature:

$$\sigma^2 = 2k_B T \lambda \tag{1}$$

The average energy gap of the backward reaction is $\Delta G_0 - \lambda$, so that the difference of the average energy gaps of the forward and backward reactions, called the Stokes shift ΔX, is equal to 2λ. The equality

$$\Delta X = \beta \sigma^2 = 2\lambda \tag{2}$$

thus provides a direct test of the picture of Gaussian bath fluctuations, $\beta = 1/(k_B T)$.

Despite its obvious importance for the formulation of Gaussian models of electron transport in molecular systems, the reorganization energy is often unknown experimentally for protein electron transfer in general and for photosynthetic electron transfer in particular. This situation distinguishes λ from the reaction free energy ΔG_0 often available from electrochemical measurements. Measurements of λ can be achieved when spectroscopy of charge-transfer bands can be recorded,[4] which is mostly not the case for protein and photosynthetic electron transfer. As a result of this lack of experimental database, the reorganization energy of photosynthetic electron transfer has become an adjustable parameter of fitting theories of radiation-

* To whom correspondence should be addressed. E-mail: dmitrym@asu.edu.
† Arizona State University
‡ Current address: University of Pennsylvania, Laboratory for the Research on the Structure of Matter.

Energetics of Bacterial Photosynthesis

J. Phys. Chem. B, Vol. 113, No. 36, 2009 **12425**

less transitions to observed reaction rates.[5,6] The resulting best-fit reorganization energies for primary charge separation have evolved over the years from very low magnitudes $\approx 0.06-0.1$ eV in earlier studies[7-9] to 0.19 eV later on,[10] and to a noticeably larger magnitude of 0.35 eV in more recent fits.[11]

The situation with the available database of electron-transfer reorganization parameters has improved in the recent decade with the widespread of numerical simulations of biological systems. A few estimates of the reorganization energy have followed, which were mostly limited to relatively short simulations,[12-15] with the exception of the recent $\simeq 3.5$ ns simulations by Marchi and co-workers.[16-18] These data gave values of the nuclear reorganization energy in the range $\simeq 0.1-0.3$ eV, close to those from original fits of experimental rates to theories of radiationless transitions.

On a more fundamental level, even though the picture of Gaussian electrostatic fluctuations is well established for small solutes,[19-21] its applicability to significantly larger and structurally heterogeneous protein solutes has never been thoroughly tested. Previous reports present conflicting results ranging between its severe breakdown (about two times ratio between λ values from the Stokes shift and from the Gaussian width[15]) and a reasonable performance.[18] This test is, however, well overdue, since the interpretation of the majority of experimental photosynthetic data has been performed by adopting the Marcus theory.[7-11]

Several potential problems make looking at the foundations of the energetics of photosynthetic electron transfer a timely direction of theoretical research. First, the time of primary charge separation, in the picosecond range, is obviously shorter than relaxation times of many modes of the protein matrix[22] and, probably, of the protein/water interface[23] relaxing on the time scale of hundreds of picoseconds to nanoseconds, or even on longer time scales.[24] The question that this observation poses is to what extent the equilibrium reaction free energy ΔG_0 can be used to characterize the vertical separation of the parabolas' minima and whether the equilibrium reorganization free energy λ, obtained from the canonical ensemble, is a proper parameter to determine the parabolas' curvatures.

The second, no less serious, question was posed by our recent observation that the reorganization energy of protein electron transfer extracted from the Gaussian width (second cumulant of the energy gap, eq 1) significantly exceeds the reorganization energy from the Stokes shift (the difference of two first cumulants of the energy gap).[25,26] This observation, implying a severe breakdown of eq 2, immediately indicates that the two-parameter description of the electron-transfer energetics (density of states) in terms of λ and ΔG_0 is not sufficient, and the theory is challenged to find a new set of parameters describing the reaction activation barrier.

Our previous studies of the energetics of electron-transfer reactions in media with relaxation times longer than the reaction time have allowed us to formulate a nonergodic theory of electronic transitions[27,28] which seems to reproduce the spectroscopy of optical dyes dissolved in low-temperature glass-forming liquids.[29] The application of this theory to our first set of simulations of the *Rb. sphaeroides* bacterial reaction center[30] has also given a good agreement with the available experimental database, in particular with recent experimental traces[11] of the population decay of the photoexcited special pair. The nonergodic cutoff of the frequencies of nuclear fluctuations permitted on the short time scale of primary charge separation reduced the reorganization energy of the first electron hop, $(P-B_L)^* \rightarrow P^+-B_L^-$, from the equilibrium value of 1.6 eV to a much smaller
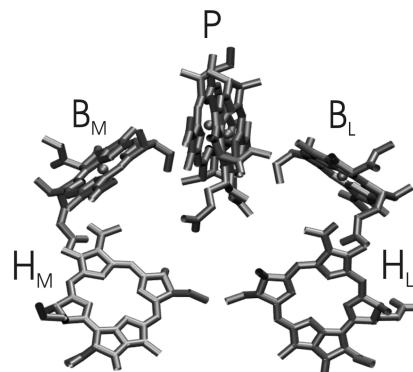

Figure 1. Schematic arrangement of cofactors in the bacterial reaction center. P is the special pair, and B and H are monomeric bacteriochlorophylls and bacteriopheophytins, respectively. Electron transfer in wild-type reaction centers occurs almost exclusively along the L-branch of cofactors (subscript "L"), while the M-branch (subscript "M") is mostly inactive.

value of 0.45 eV. Since a similar reduction applies to the nuclear solvation component of the reaction free energy, one has to conclude that thermodynamic parameters, often available from electrochemistry, cannot be used without correction to describe the activation barrier of primary charge separation.

The equilibrium reorganization energy of charge separation, obtained by us[30] from simulation trajectories much longer then in previous studies,[12,13,15-18] turned out to be significantly higher than all previous estimates in the literature, both from fitting the experimental rates and from shorter numerical simulations. Its value is, however, consistent with the gigantic reorganization energy of electron transfer in redox proteins found by us[25,26] and by some other groups.[21,31] It also turned out that the reorganization energy of 1.6 eV from the Gaussian width σ of the energy gap distribution (eq 1) far exceeds the corresponding value of 0.55 eV from the Stokes shift. Our simulations thus confirmed a qualitatively similar breakdown of the Gaussian picture previously reported by Parson et al.[15] and also point to a possibility that this type of disparity might be a general property of the electrostatic noise produced by the protein/water interface.[26]

The present paper aims to explore if the observation of significant nonergodicity effects and the breakdown of the Gaussian fluctuations picture, previously established for the first electron hop from the photoexcited special pair to the accessory bacteriochlorophyll B_L,[30] can be extended to the second hop from B_L to bacteriopheophytin H_L. The schematic arrangement of the L- and M-branch cofactors within the reaction center protein is depicted in Figure 1. In addition to primary charge separation from P to H_L, we study here the recombination kinetics from H_L to the ground state of the special pair and also try to get the first glimpse at the energetics of the primary charge separation along the M-branch of the reaction center. This channel of electronic transport is much slower than that along the L-branch,[32] and the origin of this kinetic asymmetry is still debated.[33-35]

We start with analyzing the general principles of electron-transfer energetics and what nonergodicity, caused by ultrafast primary charge separation, brings to the picture. This phenomenology serves to guide which parameters need to be used in the calculations of the reaction rates. This is followed by the discussion of the model of the reaction center and a brief account of the simulation protocol. We next present the resulting free energy surfaces of electronic transitions and fits to experimental reaction rates, followed by the discussion of the temperature

dependence of the primary recombination rate. The paper is concluded with the discussion of the results and possible extensions of new mechanistic principles uncovered here to the operation of artificial photovoltaic/photosynthetic units.

Energetics of Nonergodic Electron Transfer

The description of radiationless transitions in molecular systems is commonly formulated in terms of the multivariable reaction coordinate given by the difference in energies of the acceptor, $E_2(Q)$, and donor, $E_1(Q)$, electronic states at an instantaneous nuclear configuration of the system described by the manifold of nuclear coordinates Q: $X = \Delta E(Q) = E_2(Q) - E_1(Q)$. The free energy surfaces required to formulate the activated kinetics are then given as partial traces (Landau functionals) of the equilibrium density matrix separating the hypersurface $X = \Delta E(Q)$:

$$e^{-\beta F_i(X)} \propto \int \delta(X - \Delta E(Q)) e^{-\beta H_i(Q)} \, dQ \qquad (3)$$

Here, H_i is the system Hamiltonian in either the donor ($i = 1$) or acceptor ($i = 2$) state. Since we use the canonical ensemble, F_i denotes the Helmholtz free energy, in contrast to the Gibbs free energy experimentally available from constant-pressure measurements.

A Gaussian description of the system nuclear fluctuations leads to Marcus parabolas:

$$F_1(X) = \frac{(X - X_0)^2}{4\lambda_1}$$
$$F_2(X) = \frac{(X - X_0 + \Delta X)^2}{4\lambda_2} + \Delta F_{12} \qquad (4)$$

where ΔF_{12}, the reaction free energy for $1 \rightarrow 2$ transition, is the vertical separation between the parabolas' minima and ΔX, the reaction Stokes shift, is the horizontal separation between the minima with the coordinates X_0 and $X_0 - \Delta X$.

If the canonical ensemble is used to obtain the free energy surfaces, as in eq 3, an additional condition of energy conservation follows, $F_2(X) = F_1(X) + X$. This condition applied to eq 4 results in the standard Marcus relation between the parameters:

$$\lambda_1 = \lambda_2 = \lambda, \quad \Delta X = 2\lambda, \quad X_0 = \Delta F_{12} + \lambda \qquad (5)$$

What we have encountered in the present and previous[25,26,30] simulations is a severe breakdown of the Marcus relation (eqs 2 and 5) between the reaction Stokes shift and the reorganization energy for protein electron transfer. In the simulations, the Stokes shift is calculated from the difference of average reaction coordinates

$$\Delta X = \langle X \rangle_1 - \langle X \rangle_2 \qquad (6)$$

and the reorganization energy is calculated from the second cumulant of the reaction coordinate

$$\lambda_i = (\beta/2)\langle (\delta X)^2 \rangle_i \qquad (7)$$

In both cases, $\langle ... \rangle_i$ denotes an average over the configurations in equilibrium with the system in its ith electronic state.

Two reasons may cause the breakdown of the two-parabolas picture: (1) The system in numerical simulations is nonergodic, and the linear connection between $F_1(X)$ and $F_2(X)$, valid for the canonical ensemble, does not apply.[15] (2) The nuclear fluctuations are truly non-Gaussian, producing non-parabolic shapes of the free energy surfaces.

Nonergodicity is certainly a significant part of the problem when bacterial charge transfer occurs on the time scale much shorter than relaxation times of many nuclear modes seen in MD simulations. The problem of nonergodic kinetics can be resolved by departing from the canonical ensemble of Gibbs statistical mechanics in the definition of the reaction free energy surfaces.[36] Instead, one has to resolve to using a dynamically restricted ensemble which defines the phase space available for statistical average based on the time scale of the reaction. Specifically, one requires that Fourier transforms $Q_\omega = Q(\omega)$ of the dynamic variables $Q(t)$ do not participate in the statistical average for frequencies ω below the reaction rate k. At $\omega < k$, nuclear modes Q_ω are restricted to their frozen values Q_f, thus the name "restricted ensemble". The free energy surfaces along the reaction coordinate then become functions of k and are given by the following equation

$$e^{-\beta F_i(X,k)} \propto \int \delta(X - \Delta E(Q)) e^{-\beta H_i(Q)} \prod_{\omega < k} \delta(Q_\omega - Q_f) \prod_\omega dQ_\omega \qquad (8)$$

For nonexponential decay of the reactants' population, the rate k in eq 8 is defined as the slope of the initial population decay,[30] and that is how the reaction rate is understood throughout below.

As a result of applying the phase-space restriction in eq 8, nuclear solvation affecting the activation barrier becomes a function of the reaction rate. In particular, the nonergodic reorganization energy $\lambda(k)$ is reduced by the nonergodicity parameter[27] $f^{NE}(k) \leq 1$

$$\lambda(k) = \lambda^{eq} f^{NE}(k) \qquad (9)$$

where λ^{eq} is the equilibrium reorganization energy calculated from the canonical ensemble average. The nonergodicity correction follows from the Stokes shift time correlation function

$$S(t) = \langle \delta X(t) \delta X(0) \rangle / \langle (\delta X(0))^2 \rangle \qquad (10)$$

where $\delta X(t) = X(t) - \langle X \rangle$ and we do not specify the state in the average, since $S_1(t) = S_2(t)$ in the linear response. Specifically, the restriction of the fluctuation spectrum by fast modes only in eq 8 results in a stepwise filter imposed on the Fourier transform $S(\omega)$ in the relation for the nonergodicity correction:

$$f^{NE}(k) = 2 \int_k^\infty S(\omega) \, d\omega \qquad (11)$$

In addition to modifying the reorganization energy, nonergodicity splits the average energy gap X_0 into a sum of two components: the energy gap $X_f(k)$ produced by the nuclear modes Q_f frozen on the reaction time k^{-1} and the shift $X(k)$ produced by fast nuclear modes, which therefore can be calculated from the standard recipes of the equilibrium statistical mechanics

Energetics of Bacterial Photosynthesis

J. Phys. Chem. B, Vol. 113, No. 36, 2009 **12427**

$$X_0(k) = X_f(k) + X(k) \tag{12}$$

To simplify the notation, we have included in $X_f(k)$, apart from frozen nuclear solvation, the energy gap ΔE_0 which incorporates several additional contributions. The first component of ΔE_0 is the difference of electron affinity and ionization potential of the acceptor and donor sites, including the inhomogeneous field created by the partial charges of the protein matrix. The second component of ΔE_0 is fast electronic solvation by the electronic degrees of freedom of the medium (protein and water) incorporated into the induction shift ΔE^{ind}.

Despite the modifications of the reorganization energy and the average energy gap caused by freezing in of the slow degrees of freedom, linear solvation relations (eq 5) characteristic of the Marcus theory still hold. In particular, the frozen component cancels from the difference of average energies and $\Delta X(k) = 2\lambda(k)$. Also, the reaction free energy is now a sum of the frozen shift and equilibrium solvation by the fast nuclear degrees of freedom

$$\Delta F_{12}(k) = X_f + \Delta F(k) \tag{13}$$

where $\Delta F(k) = X(k) - \Delta X(k)/2$.

This consideration suggests that breaking ergodicity in a linearly solvating, Gaussian medium does not introduce the kind of non-Gaussian effects we observe in our simulations (refs 25 and 26 and below). We therefore have to conclude that nuclear fluctuations of hydrated proteins result in fundamentally non-Gaussian, non-parabolic free energy surfaces when projected on a single reaction coordinate. Since global shapes of these surfaces are currently unknown, it is not entirely clear how to deal with the problem and to formulate the energetics of bacterial photosynthesis. We however found empirically that the free energy surfaces can be reasonably approximated by parabolas in the range of data available from simulations. Since most of the reaction barriers encountered in photosynthesis are small, the local parabolic approximation often suffices for locating the activated state (see, however, the discussion of the primary recombination rates below). We will therefore use eq 4 with reorganization energies λ_i obtained from either fitting the free energy curves or from eq 7 with the provision that these free energy curves are just approximate representations of some unknown, globally non-parabolic surfaces for which the relations listed in eq 5 do not hold anymore.[28] The condition $F_1(0) = F_2(0)$ still locates the activated state $X = 0$ and is used to extract the reaction barrier and the reaction free energy ΔF_{12}.

Because of the breakdown of the Gaussian fluctuations picture, our use of the derivation presented here to gain access to nonergodic reorganization parameters is somewhat limited. We will therefore rely more on an empirical approach of producing shapes of the free energy surfaces by applying a narrow observation window to the simulation trajectories, as described below. Since this procedure does not address the question of how to calculate the nonergodic average shift $X_0(k)$ in eq 12, Stokes shift dynamics from MD will still be used to obtain the nonergodic correction (eq 11) and the dependence on the reaction rate k in $X_0(k)$.

Model

We model primary bacterial charge separation by four distinct electronic states shown in Figure 2. The ground-state special pair P (state 0) is lifted to the photoexcited state P* (state 1) by absorption of a photon of visible light. This is followed by the first electron hop to the accessory bacteriochlorophyll to form
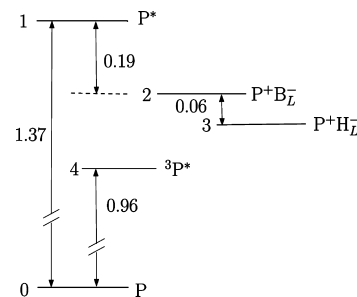

Figure 2. Electronic states involved in primary charge separation and recombination. Vertical arrows indicate the equilibrium free energy gaps (in eV, at 300 K) and energies of optical transitions. The gaps for the special pair photoexcitation to the singlet and triplet states are taken from experiment.[10] The other two gaps are the equilibrium free energy gaps calculated in this paper. They are not equal to the nonergodic reaction energies realized on the reaction time scale, as is explained in the text.

the charge-separated state $P^+ - B_L^-$ (state 2). The next electron hop to bacteriopheophytin produces $P^+ - H_L^-$ (state 3). State 3 can recombine to the original ground state P on the nanosecond time scale.[10] An additional recombination channel of state 3 is to a photoexcited triplet of the special pair, $^3P^*$ (state 4). The energy gaps between P and P* and between P and $^3P^*$ are known from experimental spectroscopic measurements,[10] while the free energy gaps between other states shown in Figure 2 are from our calculations described below.

The modeling of the photoexcited state of the special pair deserves special comment. Stark spectroscopy data recorded at 77 K indicate a very substantial change in the special pair's polarizability, of about 460–750 Å³, upon photoexcitation.[37] This very large polarizability change, which places the photoexcited special pair among the most polarizable molecules known, is related to electronic delocalization between the neutral, $(P_M - P_L)^*$, and ionized, $(P_M^+ - P_L^-)^*$, states of the bacteriochlorophyll sandwich,[38] where P_M and P_L are, correspondingly, the M and L subunits of the special pair. Physically, it implies that the charge distribution of the special pair will readjust between the neutral and ionized states at each instantaneous nuclear configuration of the system. We account for this readjustment by defining the atomic charges of the special pair as $z_j^P + n_{\text{CT}}\Delta Z_j$, where z_j^P are the atomic charges of the neutral state, ΔZ_j are the differences of atomic charges between the ionized and neutral states, and j runs over the atoms of the special pair. The atomic charges in neutral, positive, and negative bacteriochlorophyll molecules required for this parametrization were calculated at the B3LYP DFT/3-21G level and tabulated in our previous publication.[30] The population of the ionized state n_{CT} shows how much ionic character the special pair has at a particular nuclear configuration. This parameter is obtained as a solution of the two-state Hamiltonian and is updated at each fifth step of the MD trajectory. The parameters of the two-state Hamiltonian of the special pair are chosen to reproduce the polarizability of the photoexcited state reported from Stark spectra at 77 K[37] and then adjusted to be used at 300 K. More details on the parametrization are given in the Appendix, and the details of implementing the MD protocol can be found in the Supporting Information.

The other three states of the charge separation scheme (states 0, 2, and 3) are nonpolarizable, with the atomic charges fixed by the DFT calculations. The atomic charges of H_L and H_L^-, also obtained at the B3LYP DFT/3-21G level, are tabulated in the Supporting Information. For the charge-separated states, the positive charge on P^+ is unequally distributed between P_L and P_M, with $^2/_3$ of the positive charge on P_L and $^1/_3$ of the positive charge on the P_M subunit, as suggested by ENDOR studies of

TABLE 1: Components of the Average Energy Gap and Reorganization Energy (All Energies Are in eV, $T = 300$ K)

transition branch	$1 \rightarrow 2$ L	$1 \rightarrow 2$ M	$2 \rightarrow 1$ L	$2 \rightarrow 1$ M	$2 \rightarrow 3$ L	$3 \rightarrow 2$ L	$3 \rightarrow 2$ L(-Fe)[a]	$0 \rightarrow 3$ L	$3 \rightarrow 0$ L	$3 \rightarrow 0$ L(-Fe)[a]
					Average Energy Gap					
$\Delta E_{\mathrm{w}}^{\mathrm{ind}}$	−0.05	−0.07	−0.08	−0.05	−0.08	−0.04	0.11	−0.08	−0.08	−0.09
$\Delta E_{\mathrm{prot}}^{\mathrm{ind}}$	−0.98	−1.26	−1.07	−1.09	−0.48	−0.40	−0.47	−1.07	−1.05	−0.94
ΔE^{ind}	−1.03	−1.34	−1.15	−1.14	−0.56	−0.44	−0.37	−1.15	−1.13	−1.03
$\Delta E_{\mathrm{w}}^{\mathrm{C}}$	0.33	−0.03	−0.37	−0.36	0.54	0.03	−0.27	0.54	−0.16	−0.02
$\Delta E_{\mathrm{prot}}^{\mathrm{C}}$	−0.56	0.18	−1.28	−0.76	0.09	−0.95	−1.11	−1.15	−2.24	−2.57
ΔE^{C}	−0.24	0.15	−1.64	−1.12	0.63	−0.92	−1.38	−0.61	−2.40	−2.60
$\Delta E_{\mathrm{s}}^{b}$	−1.26	−1.19	−2.80	−2.26	0.07	−1.35	−1.75	−1.76	−3.53	−3.63
					Reorganization Energy					
λ_{prot}	0.69	2.25	0.59	0.65	0.70	0.75	0.54	0.57	1.37	0.65
λ_{w}	1.48	2.06	1.38	1.89	1.93	0.96	0.80	1.92	1.79	2.64
λ	2.36	4.98	1.69	2.92	2.49	1.98	1.07	2.24	2.85	2.72
τ_{sim}^{c}	10	10	10	10	10	5.5	4.5	10	5.5	4.5

[a] Simulations with nonheme iron absent from the protein matrix. [b] $\Delta E_{\mathrm{s}} = \Delta E^{\mathrm{ind}} + \Delta E^{\mathrm{C}}$ is the solvent-induced shift of the donor−acceptor energy gap. [c] The length of the simulation trajectory (in ns).

Rb. sphaeroides.[39] The atomic charges of the cofactors are used to calculate their Coulomb interaction with the protein matrix modeled by the Amber FF03 force field[40] and with water given by the TIP3P force field.[41]

The constant charges of the force fields are used to run MD trajectories and to calculate the Coulomb component $\Delta E_{ij}^{\mathrm{C}}(Q)$ of the instantaneous donor−acceptor energy gap

$$X_{ij}(Q) = \Delta E_{ij}^{\mathrm{gas}} + \Delta E_{ij}^{\mathrm{ind}}(Q) + \Delta E_{ij}^{\mathrm{C}}(Q) \qquad (14)$$

where $i, j = 0, 1, 2, 3, 4$ denote the two states between which the gap is calculated. In this notation, for instance, $X_{12}(Q)$ denotes the instantaneous value of the reaction coordinate for the first electron transfer, P−B$_{\mathrm{L}}$ → P$^+$−B$_{\mathrm{L}}^-$ (Figure 2). The average of the reaction coordinate $X_{ij}(Q)$, normally corresponding to the minimum of the electron-transfer free energy surface, will be denoted as $X_{0,ij} = \langle X_{ij} \rangle_i$. Here, index i stands for both the initial state of electronic transition and the state used to calculate the statistical average.

The atomic charges of the cofactors are used to calculate the average Coulomb shift of the reaction coordinate $\Delta E_{ij}^{\mathrm{C}}$ and also to calculate the electric field $\mathbf{E}_i$ of the entire set of cofactors in each state $i = 0, 1, 2, 3, 4$. These fields are then incorporated into the average induction component of the donor−acceptor energy gap

$$\Delta E_{ij}^{\mathrm{ind}} = -\left\langle \sum_k (\alpha_k/2)[\mathbf{E}_j^2(\mathbf{r}_k) - \mathbf{E}_i^2(\mathbf{r}_k)] \right\rangle_i \qquad (15)$$

Here, $\langle ... \rangle_i$ denotes an ensemble average over the nuclear configurations of the system in equilibrium with the electronic state $i = 0, 1, 2, 3, 4$ and the sum runs over all atoms of the protein and water with positions $\mathbf{r}_k$ and polarizabilities α_k. Finally, $\Delta E_{ij}^{\mathrm{gas}}$ in eq 14 refers to the difference of the ionization potential of the donor cofactor and the electron affinity of the acceptor cofactor in the gas phase, without the electrostatic effect of the permanent and induced charges of the protein/water solvent. The average energy gap is therefore a sum of the gas-phase, induction, and Coulomb components

$$X_{0,ij} = \Delta E_{ij}^{\mathrm{gas}} + \Delta E_{ij}^{\mathrm{ind}} + \Delta E_{ij}^{\mathrm{C}} \qquad (16)$$

The atomic polarizabilities α_k in eq 15 were taken from Thole's parametrization.[42] The induction interactions were not a part of the simulation protocol, thus assuming that the nuclear configurations of the system are adequately sampled with the standard force fields. Since the force fields effectively include atomic and molecular polarizabilities in their permanent charges, they were multiplied by an empirical factor of 0.89 in analyzing the data to avoid double counting of the polarizability effects, following the practice adopted in the literature.[16,18,43]

The results of MD simulations calculated on full 10 ns trajectories are presented in Table 1. In order to provide mechanistic insights into the factors affecting electronic transitions, the average energy gaps listed there are split into the contribution from induction and Coulomb interactions, each of them additionally separated into the water (subscript "w") and protein (subscript "prot") components. As we also found previously,[30] the induction interactions (mostly with the protein) make the major contribution to the solvent-induced shift of the average energy gap. The induction forces contribute little, compared to the Coulomb interactions, to the reorganization energy, since they mostly produce a mean-field energy shift disappearing in the variance. The equilibrium reorganization energy is dominated by water, but this contribution is strongly cut off by nonergodicity effects at short time scales of the transition.[30]

Our simulations have shown that the nonheme iron atom is not stable for long MD runs in the charge-separated state P$^+$−H$_{\mathrm{L}}^-$ and leaves the protein matrix after about 5.5 ns of simulations. The data shown in Table 1 are therefore produced from two separate pieces of the trajectory, with and without an iron atom present in the protein. Although there are some differences in the reported reorganization parameters, we could not identify any dramatic mechanistic changes introduced by this alteration of the protein composition.

Charge-Transfer Transitions

Most of the simulation data reported here were done for the L-branch cofactors with their energetics shown in Figure 2. We have, however, also analyzed the statistics of energy gap fluctuations for the primary electron hop to B$_{\mathrm{M}}$, and have run an additional simulation of the P$^+$−B$_{\mathrm{M}}^-$ configuration in order to determine the complete energetics of this transition. The results of all of these simulations are summarized in Table 1 which reports the average energy gaps and reorganization
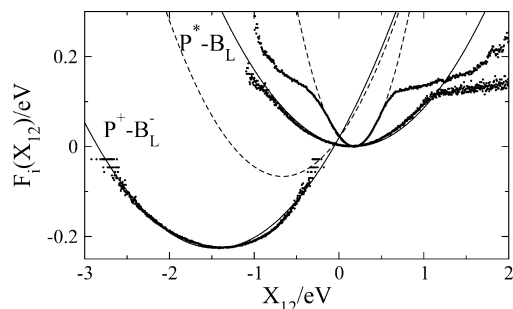
Energetics of Bacterial Photosynthesis

J. Phys. Chem. B, Vol. 113, No. 36, 2009 **12429**

Figure 3. $F_1(X_{12})$ and $F_2(X_{12})$ free energy surfaces for the first electron hop of primary charge separation. The two upper sets of points represent MD simulations on the entire 10 ns trajectory (broader curve) and on the 4 ps observation window (narrower curve). The lower set of points represents the $F_2(X_{12})$ surface obtained from the 10 ns trajectory of the charge-separated state $P^+-B_L^-$. The solid and dashed upper curves are fits of the lower, parabolic portions of the simulated data to parabolas. The solid lower curve is a fit of the simulated surface $F_2(X_{12})$ to the Q-model[44] allowing asymmetry of the free energy surface. The coinciding positions of the minima of the $F_1(X_{12})$ curves were obtained to make the 4 ps curve reproduce the experimental activation barrier $F_1(0,k_{12})$. $V_{12} = 41.5$ cm^{-1} was used in the rate calculation.

energies obtained from variances of the corresponding reaction coordinates (eq 7).

$P^*-B_L \rightarrow P^+-B_L^-$ Transition. The free energy surfaces for the $1 \rightarrow 2$ and $2 \rightarrow 1$ transitions between the photoexcited special pair and the accessory bacteriochlorophyll B_L are shown in Figure 3. The two broader distributions indicated by points refer to the histograms obtained from 10 ns simulation trajectories. The solid lines are fits of lower parts of these histograms, close to their minima, to parabolas (eq 4). The dashed curves and the upper narrower set of points are nonergodic free energy surfaces corresponding to a 4 ps observation window. The nonergodic free energy surface of the P^*-B_L state was calculated directly from the simulation trajectory. More specifically, the histogram of energy gaps was obtained by sliding a 4 ps observation window along the trajectory, followed by averaging of separate histograms over all observation windows with their maxima shifted to a common position. This calculation allows us to address the effect of nonergodicity on the free energy's shape, but not on the average donor−acceptor energy gap. The latter value is fixed by fitting the charge-transfer rate to experiment.

Photoexcitation of the special pair occurs from the ground-state configuration in equilibrium with the surrounding protein/water medium. If one assumes that this transition does not change the electric field of the special pair dramatically,[15] the initial state for the first electron hop finds itself in an equilibrium distribution of the nuclear configurations. Even if this reaction occurs on a very short time scale, the average energy gap on that time scale ($X_0(k)$ in eq 12) is equal to the equilibrium average gap X_0. The reaction nonergodicity therefore does not affect the average energy gap, and the free energy surface can be adopted in the form

$$F_1(X_{12},k) = \frac{(X_{12} - X_{0,12})^2}{4\lambda_{12}(k)} \quad (17)$$

Here, following eqs 14 and 16, we use a somewhat more complex notation scheme than above. Since we need to distinguish between the activation parameters of, for instance, $2 \rightarrow 1$ and $2 \rightarrow 3$ transitions, both the reorganization energy and the average energy gap carry two indices ij, where the first

index i designate the thermodynamic state used to calculate the statistical averages and the second index indicates the direction of the reaction. At the same time, the lower index in the free energy function specifies the canonical ensemble in equilibrium with the electronic state $i = 0, 1, 2, 3, 4$ of the reaction center.

The value of $\lambda_{12}(k)$ in eq 17 is obtained from fitting the 4 ps surface in Figure 3 to a parabola, which results in 0.36 eV, much lower than the reorganization energy 2.36 eV obtained from the entire 10 ns trajectory (Table 1). This latter equilibrium reorganization energy is also higher than the corresponding value of 1.6 eV from our simulations[30] employing fixed charges only. This result is expected, since highly polarizable molecules can significantly modify the reorganization energy.[28] The value of 2.36 eV is also slightly below 2.51 eV previously reported by us[30] because of the changes in the parametrization of the two-state Hamiltonian implemented here to better conform with the experimental database (Appendix).

The free energy surface $F_1(X_{12})$ of the initial highly polarizable state 1 is also globally asymmetric (Figure 3), as expected for polarizable charge-transfer molecules,[44] but this asymmetry minimally affects the rate because of the small activation barrier. The surface $F_2(X_{12})$ of the final state 2 was also found to be slightly asymmetric, and the Q-model of electron transfer describing polarizable systems,[44] which allows such asymmetry, was used to fit the simulated curve (lower solid curve in Figure 3).

As mentioned above, the horizontal position of the free energy curve $F_1(X_{12})$ was determined by fitting the rate of nonadiabatic electronic transition to its experimental value[45,11] $k_{12}^{exp} = 3.4 \times 10^{11}$ s^{-1}. The nonadiabatic rate is given by the standard expression

$$k_{12} = \frac{V_{12}^2}{\hbar}\left(\frac{\pi\beta}{\lambda_{12}(k_{12})}\right)^{1/2} \exp[-\beta F_1(0,k_{12})] \quad (18)$$

in which the dependence on k_{12} in the rhs indicates that the reorganization energy and corresponding free energy surfaces are obtained from the calculations employing the 4 ps observation window. In this calculation, $V_{12} = 41.5$ cm^{-1} from our previous paper[30] was used, which has resulted in an average energy gap of $X_{0,12} = 0.17$ eV. When this value is used in eq 16 along with the Coulomb and induction components from MD simulations (Table 1), one gets the gas-phase splitting between P^* and B_L^- equal to $\Delta E_{12}^{gas} = 1.43$ eV.

The minimum of the $F_2(X_{12})$ surface is fixed by the Stokes shift from the simulations and the calculated shift $X_{0,12}$. The reaction free energy, the vertical separation between the minima, was obtained by imposing the condition $F_1(0) = F_2(0)$, where the free energy surface $F_2(X_{12})$ was taken in the form

$$F_2(X_{12}) = \frac{(X_{12} - X_{0,12} + \Delta X_{12})^2}{4\lambda_{21}} + \Delta F_{12} \quad (19)$$

This procedure, applied to the "equilibrium" surfaces from full 10 ns trajectories, leads to $\Delta F_{12} = -0.19$ eV (Figure 3). This magnitude is very close to the free energy gap $\Delta G_{13} = -0.25$ eV for the reaction $P^*-B_L \rightarrow P^+-H_L^-$ established experimentally.[10] If this was a correct value of the reaction free energy, the second electron hop $P^+-B_L \rightarrow P^+-H_L^-$ would proceed with a very low driving force $\simeq 0.06$ eV, a significant activation barrier, and a noticeable temperature dependence of the reaction rate, in disagreement with experiment.
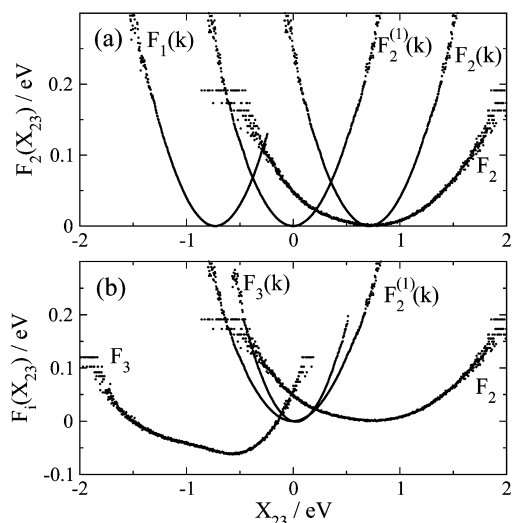
Figure 4. Upper panel: Free energy surfaces along the reaction coordinate X_{23} for the $2 \rightarrow 3$ transition. $F_1(X_{23},k)$ was obtained from MD trajectory in state 1 (Figure 2) over the 4 ps observation window. $F_2(X_{23},k)$ and $F_2(X_{23})$ were obtained from MD trajectory in equilibrium with state 2 (Figure 2) with 4 ps and 10 ns windows, respectively. The curve marked as $F^{(1)}(k)$ was obtained by shifting $F_2(X_{23},k)$ to the position of its minimum $X_{0,23}(k)$ where only fast nuclear modes have relaxed on the observation time, $k = (4 \text{ ps})^{-1}$. Lower panel: In addition to the equilibrium free energy curve $F_2(X_{23})$ and the nonergodic curve $F^{(1)}(X_{23},k)$, identical to those in the upper panel, the curves obtained from the trajectories in state 3 (Figure 2) are shown. They have been obtained from 4 ps, $F_3(X_{23},k)$, and 10 ns, $F_3(X_{23})$, observation windows. Their horizontal positions are obtained as described in the text. The equilibrium reaction free energy is obtained by imposing the condition $F_{32}(0) = F_{23}(0)$.

Clearly, the equilibrium free energy surface does not describe the reaction occurring on the picosecond time scale. We, however, do not have a direct formalism to calculate the nonergodic free energy surface $F_2(X_{12},k)$. An approximate solution can be obtained by calculating the nonergodic reorganization energy $\lambda_{21}(k) = \lambda_{21}^{eq} f_{21}^{NE}(k)$ with the nonergodicity factor $f_{21}^{NE}(k)$ from the equilibrium Stokes shift correlation function of state 2 according to eq 11. The nonergodic Stokes shift between states 1 and 2 should also be scaled with the same nonergodic function, resulting in the nonergodic surface

$$F_2(X_{12}, k) = \frac{(X_{12} - X_{0,12} + f_{21}^{NE}(k)\Delta X_{12})^2}{4\lambda_{21}(k)} + \Delta F_{12}(k)$$

(20)

The result of this calculation is shown by the lower dashed line in Figure 3, and the nonergodic reaction free energy becomes $\Delta F_{12}(k) = -0.11$ eV, about a half of the equilibrium free energy gap. The rate constant $k = (4 \text{ ps})^{-1}$ was used in this calculation for consistency with the procedure used to calculate the surface $F_1(X_{12})$ from simulations. The simulated Stokes shift time correlation function was fitted to a sum of a Gaussian and two exponents and then used for the calculation of the nonergodicity factor. The results of fits of the Stokes shift functions for transitions $i \rightarrow j$ studied here can be found in the Supporting Information.

P$^+$–B$_L^-$ $\rightarrow$ P$^+$–H$_L^-$ Transition. The calculations of the second transition step are more complex because this is a transient state and the nuclear configurations do not have a sufficient time to equilibrate on the time scale of the reaction. The issues involved are illustrated in Figure 4a. There we show four free energy surfaces plotted against the reaction coordinate X_{23}, all of them brought to

the same level of their minima. The three narrow curves were calculated on the 4 ps observation window as explained above, and the single broad curve F_2 was obtained from the entire 10 ns trajectory. The curve $F_1(X_{23},k)$ was calculated on configurations in equilibrium with state 1 (P*–B$_L$, Figure 2), in which the nuclear coordinates have not had a chance to adjust to the new charge-separated state (state 2). On the contrary, the curves $F_2(k)$ and F_2 were calculated on the trajectory of state 2 (P$^+$–B$_L^-$, Figure 2), the first one on the 4 ps observation window and the second one on the entire 10 ns trajectory. As we have mentioned above, our procedure for extracting free energies from narrow observation windows applied to the long trajectory allows us to address the shape of the curve but not the nonergodic average energy gap. Therefore, the minima of the narrow and the broad F_2 curves in state 2 coincide, corresponding to the average energy gap $X_{0,23}$.

One has to take into account that the nuclear degrees of freedom do not equilibrate on the time scale of the first electron hop and one cannot use the equilibrium MD configurations to calculate the free energy surface $F_2(X_{23},k)$. An approximate solution that we have decided to adopt is to take the portion $f_{23}^{NE}(k)\Delta X'$ of the entire shift $\Delta X'$ between the minima of $F_1(X_{23},k)$ and $F_2(X_{23},k)$ curves for the shift of the free energy surface for the second electron hop. This is shown by curve $F_2^{(1)}(X)$ in Figure 4a. The use of $f_{23}^{NE}(k)$ for this estimate might seem somewhat arbitrary, but we obtained essentially identical results with $f_{12}^{NE}(k)$ instead.

The curve $F_2^{(1)}(X_{23},k)$ was used in further calculations. This surface needs to be combined with the nonergodic surface $F_3(X_{23},k)$ for the calculation of the forward rate k_{23}. This latter was obtained from the 4 ps sliding window applied to the MD trajectory in state 3 followed by the nonergodic shift by $f_{32}^{NE}(k)\Delta X_{23}$, in accord with the procedure used for the first electron hop. The remarkable result of this calculation is that minima of $F_2^{(1)}(X_{23},k)$ and $F_3(X_{23},k)$ coincide (Figure 4b). This implies that the second transition occurs with zero driving force and no activation barrier. The experimental rate[2] of $(0.9 \text{ ps})^{-1}$ then requires the matrix element of $V_{23} = 56$ cm^{-1}, which is close to $V_{12} = 41.5$ cm^{-1} and somewhat below $V_{23} = 122$ cm^{-1} calculated by Zhang and Friesner.[33] With the induction shift of the donor–acceptor energy gap from simulations (Table 1), one then gets $\Delta E_{23}^{gas} = 1.18$ eV for the gas-phase energy gap. This latter value is used to calculate the equilibrium energy shift and to position the equilibrium free energy surfaces $F_2(X_{23})$ and $F_3(X_{23})$ along the reaction coordinate (Figure 4b). The equilibrium transition then results in a small negative reaction free energy of -0.06 eV. When this value is combined with the equilibrium reaction free energy of the first transition, one obtains $\Delta F_{13} = \Delta F_{12} + \Delta F_{23} = -0.25$ eV. This value is in remarkable agreement with the experimental[10] free energy gap of $\Delta G_{13} = -0.25$ eV measured on the nanosecond time scale comparable with the length of our simulations.

P$^+$–H$_L^-$ $\rightarrow$ P Transition. Recombination $3 \rightarrow 0$ of the charge-separated state P$^+$–H$_L^-$ to the ground state of the special pair P occurs in the inverted region of electron transfer and thus requires account for vibrational excitations of the final state. These are accounted for in the standard prescription[5] as a sum over vibronic excitations characterized by the Huang–Rhys factor[9] $S = 0.5$ and the vibrational frequency[9] $\hbar\omega_v = 1500$ cm^{-1}

$$k_{30} = \frac{|V_{30}|^2}{\hbar}\left(\frac{\pi\beta}{\lambda_{30}^{eq}}\right)^{1/2} \sum_{n=0}^{\infty} \frac{S^n}{n!} \exp\left[-S - \beta\frac{(X_{0,30} - n\hbar\omega_v)^2}{4\lambda_{30}^{eq}}\right]$$

(21)

Energetics of Bacterial Photosynthesis

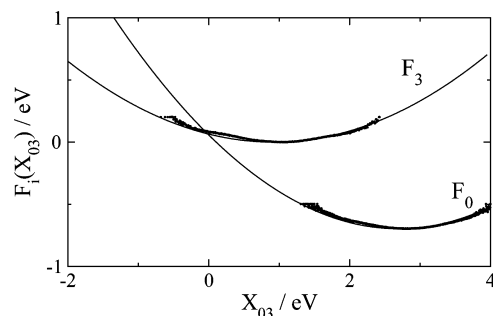*J. Phys. Chem. B, Vol. 113, No. 36, 2009* **12431**

Figure 5. $F_3(X_{03})$ and $F_0(X_{03})$ free energy surfaces. The equilibrium energy gap for the $3 \rightarrow 0$ transition was obtained by fitting the experimental rate.[10] The equilibrium Stokes shift from MD simulations was used to define the horizontal position of the surface $F_0(X_{03})$, and its vertical position was obtained from the requirement that the parabolic extrapolation of the simulation data crosses with the $F_3(X_{03})$ surface at $X_{03} = 0$. $V_{30} = 2$ cm^{-1} was used in the calculations.[33]

Figure 6. Free energy surfaces for recombination from the charge-separated state $P^+ - H_L^-$ to the photoexcited triplet of the special pair $^3P^*$. The reaction coordinate X_{43} is shifted relative to the reaction coordinate of singlet recombination X_{03} by the constant amount of 0.96 eV.

Since recombination has the experimental rate[10] of $k_{30} = 4.7 \times 10^7$ s^{-1}, no nonergodicity corrections are required in this case and the equilibrium reorganization energy λ_{30}^{eq} and equilibrium induction and Coulomb components of the solvent-induced shift in $X_{0,30}$ can be used in the rate calculations. Charge recombination occurs through a superexchange mechanism with the effective electronic coupling[33] $V_{30} = 2$ cm^{-1}.

Fitting the experimental reaction rate with the average solvent-induced shift from simulations requires a gas-phase component of the overall average energy gap equal to $\Delta E_{03}^{gas} = 4.58$ eV. If the gas-phase shifts for $1 \rightarrow 2$ and $2 \rightarrow 3$ transitions calculated above are subtracted from this magnitude, one gets $\Delta E_{01}^{gas} = 1.97$ eV, which is higher than $h\nu_{abs} = 1.37$ eV experimentally observed for the excitation of the special pair (Figure 2). The latter value is expected to be red-shifted from its gas-phase value ($h\nu_{abs} < \Delta E_{01}^{gas}$), but it is not entirely clear by how much.

The experimental recombination rate is reproduced with the average energy gap $X_{0,30} = 1.05$ eV and a low activation barrier of about 0.06 eV. However, when a parabolic extrapolation (Figure 5) is used for the lower free energy surface $F_0(X_{03})$, the resulting reaction free energy $\Delta F_{30} = -0.7$ eV comes lower in the absolute value than the experimental result, $\Delta G_{30} = -1.12$ eV.[10] All of our present results indicate that the free energy surfaces should be globally non-parabolic, and finding the crossing point between $F_0(X_{03})$ and $F_3(X_{03})$ requires an extrapolation far beyond the range of energy gaps available from simulations. This might be the reason why the parabolic extrapolation clearly fails here, and a true free energy surface should be much steeper on its left wing than a parabola.

$P^+ - H_L^- \rightarrow {}^3P^*$ Transition. Due to intersystem crossing to the triplet state of the singlet charge-separated state $P^+ - B_L^-$, an additional recombination channel exists to the photoexcited triplet of the special pair, $^3P^*$. The rate of this reaction is experimentally known to be $k_{34} = 5 \times 10^8$ s^{-1} and is nearly independent of temperature.[10] This additional piece of kinetic evidence can be used to test the consistency of our calculations of the recombination rate. The energy gap of 0.41 eV between $^1P^*$ and $^3P^*$ was determined from fluorescence and phosphorescence spectra,[46] which implies a gap of $h\nu^T = 0.96$ eV between $^3P^*$ and P (Figure 2). Therefore, the reaction coordinate for the triplet recombination X_{43} is shifted by this amount relative to the reaction coordinate for singlet recombination X_{03}: $X_{03} = X_{43} + h\nu^T$. The corresponding free energy surface $F_3(X_{43})$ is then obtained by a simple horizontal shift of the curve $F_3(X_{03})$ in Figure 5, as is shown in Figure 6. This surface then crosses the transition state $X_{43} = 0$ with almost no barrier, which is of
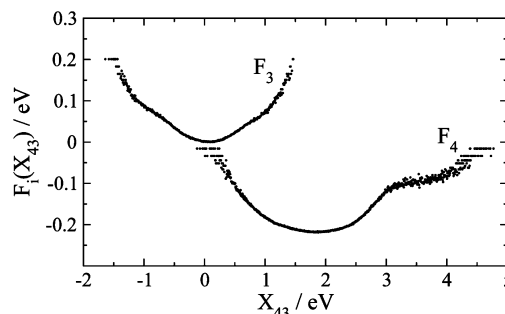
course consistent with the experimentally observed weak temperature dependence of triplet recombination.[10] Moreover, when the recombination rate is calculated with[33] $V_{30} = 2$ cm^{-1} used above for singlet recombination, the resulting value of 5.4×10^8 s^{-1} is in very good agreement with experiment.

The placement of the second electron-transfer surface $F_4(X_{43})$ in Figure 6 is more uncertain. We have no information on the polarizability of the photoexcited triplet, and our two-state model used in the simulations was designed to reproduce the experimental data for the photoexcited singlet. We, however, tentatively calculated the distribution of the reaction coordinates X_{43} on the configurations obtained for state 1. This surface, marked as F_4, is also shown in Figure 6. The reaction free energy from this calculation is -0.22 eV, compared to -0.16 eV from experiment.[10]

$P^* - B_M \rightarrow P^+ - B_M^-$ Transition. Despite approximate geometrical symmetry between the L- and M-branches of cofactors in the reaction center (Figure 1), electron transfer is highly asymmetric, proceeding almost exclusively along the L-branch. The rate of electron transfer to H_M is about 200 ps, as opposed to 3 ps for the transfer to H_L.[32] This puzzling observation has received significant attention, both experimentally[34,35] and theoretically[33] (see ref 47 for a review). Most explanations focus on either the asymmetry in the reaction free energies between L and M pathways or on the difference in the electronic coupling.[33] Different energetics might be attributed to either the large-scale dielectric asymmetry of the protein matrix[48,49] or to local variations of bonding between cofactors and their nearest aminoacids.[50] Although all of these factors might contribute to the net effect, one possibility has not received much attention, that is, the asymmetry in the reorganization energy. This possibility needs to be considered given a large polarizability of the photoexcited special pair.[37] Since this polarizability mostly comes from electronic coupling between two sandwiched bacteriochlorophylls, the corresponding polarizability tensor is highly anisotropic. The overall solvent reorganization energy is proportional to the average squared of the sum of the permanent, $\mathbf{m}_{CT}$, and induced, $\mathbf{p}$, electron-transfer dipoles, $\lambda \propto \langle (\mathbf{m}_{CT} + \mathbf{p})^2 \rangle$.[44] Since the induced dipole is significant in highly polarizable systems, its direction relative to the permanent dipole, determined by the polarizability tensor, might affect the overall reorganization energy, as we indeed observe here.

Since the transition along the M-branch occurs on a much longer time scale of about 200 ps,[47] full 10 ns simulation trajectories are used to calculate the free energy surfaces of the reaction. Our simulations here are limited to states 1 and 2 M ($P^+ - B_M^-$), and we plot the free energies along the reaction coordinate X_{12}^M obtained as the instantaneous energy gap between
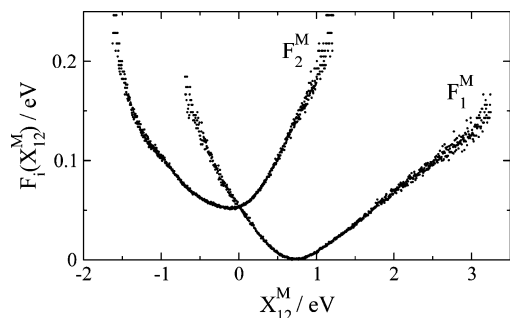
Figure 7. $F_1^M(X_{12}^M)$ and $F_2^M(X_{12}^M)$ obtained from MD simulations. The position of the minimum of the F_1^M surface was adjusted to reproduce the experimental time of charge separation of 200 ps. The F_2^M surface was shifted vertically and horizontally to reproduce the Stokes shift ΔX_{12}^M from simulations and to ensure the condition $F_1^M(0) = F_2^M(0)$.

states 1 and 2 M (Figure 7). The free energy surface $F_1^M(X_{12}^M)$ is clearly asymmetric, with the type of asymmetry anticipated by the Q-model of electron transfer developed to describe charge transfer in highly polarizable donor−acceptor complexes.[44] The free energy $F_2(X_{12}^M)$ is more symmetric, since the corresponding configurations were produced on cofactors with fixed charges and no polarizability.

The equilibrium reorganization energy of 5 eV along the M-branch is about twice larger than the corresponding equilibrium reorganization energy along the L-branch (Table 1). Given the nonergodicity reduction of the latter value down to 0.36 eV, we have here an order of magnitude difference in the reorganization energies between the two branches. Of course, some energetic factors should contribute to a longer time scale of M-side electron transfer to allow nuclear solvation to develop and produce a larger reorganization energy. There is little asymmetry in the induction shift between the two branches (Table 1), since this solvation component basically reflects the density of polarizable groups in the cofactors' vicinity. On the other hand, both water and protein Coulomb solvation energies have opposite signs for the two branches. In particular, the electrostatic shift by the protein matrix differs by 0.74 eV between L- and M-branches. The electrostatic protein environment thus promotes charge transfer along the L-branch and prohibits it along the M-branch. While this conclusion is in accord with some experimental evidence,[48,49] the net electrostatic effect on the average donor−acceptor energy gap is small compared to the dominant induction shift (Table 1), and the total solvent-induced shift is nearly identical for the two branches. The same is true for the backward transition 2 M → 1. Therefore, it is the local effect of binding between protein's aminoacids and the cofactors, incorporated into ΔE^{gas} in our description, that breaks the symmetry of charge transfer.

The fit of the simulated free energy curve to the experimental transfer time of 200 ps supports this conjecture. The average energy gap that allows reproduction of the rate of $(200 \text{ ps})^{-1}$ appears to be $X_{0,12}^M = 0.69$ eV, compared to $X_{0,12}^L = 0.17$ eV for the L-branch. This makes the gas-phase gap $\Delta E_{12}^{gas,M} = 1.87$ eV, which is 0.44 eV higher than the corresponding gap along the L-branch. The electronic coupling between the special pair and B_M of $V_{12}^M = 17 \text{ cm}^{-1}$ from Zhang and Friesner[33] was used in this calculation. We need to stress that the rate used in these calculations refers to the electron hop to H_M known only approximately for the wild-type reaction center.[47] The rate for the electron transfer to B_M is unknown, and the calculations presented here are bound to some uncertainty. Nevertheless, we found that the $F_2(X_{12}^M)$ curve is lifted compared to the $F_1(X_{12}^M)$ curve, resulting in the reaction free energy $\Delta F_{12}^M = 0.05$ eV.

Given the approximate value for the rate, this number seems to be in reasonable agreement with the experimental estimate, also resulting in a positive reaction free energy of about $\Delta G_{12}^M \simeq 0.1-0.15$ eV.[35] The striking result of this calculation is that the backward 2 M → 1 transition is nearly activationless (Figure 7). If this result is correct, the actual electronic transition to H_M might occur through the superexchange mechanism.

The superexchange scenario might provide one possible explanation that a noticeable barrier for the 1 → 2 M reaction obtained here is apparently inconsistent with the recent observation of about 2 times increase in the rate when the temperature is lowered from 295 to 77 K.[35] However, an alternative explanation can be offered as well. It appears that an increase of the rate with lowering temperature is a universal feature of primary charge separation, common to both L and M 1 → 2 transitions and to transition to the L-quinone cofactor.[51] Since this feature is common to reactions separated by 2 orders of magnitude in their respective rates, a universal explanation might be required. What is common to all observed transitions is the dominance of the induction component in the average energy gap. This energy shift becomes more negative with lowering temperature, thus resulting in a rate increase. The temperature variation of the induction shift was sufficient to explain the observed temperature dependence of the 1 → 2 L rate.[30] Similarly, a 2 times increase of the rate when lowering temperature from 295 to 77 K, found for the 1 → 2 M reaction, requires about 10% more negative induction component of the energy gap, a change consistent with our previous simulations of the L-branch energetics at different temperatures.[30]

Temperature Dependence of the Recombination Rate. Several steps of primary charge separation accelerate with lowering temperature.[35,45,51] This observation is commonly explained by theories of radiationless transition in terms of the temperature variation of vibrational populations for near-activationless transitions.[5] In contrast to this common explanation requiring $X_0 \simeq 0$, mutagenesis experiments[52] and more recent kinetic data[11] yield a substantial positive average energy gap $X_0 > 0$ placing primary charge separation into the Marcus normal region of electron transfer. The magnitude of the average energy gap, $X_{0,12} = 0.17$ eV, is inconsistent with the small temperature dependence of the rate if used in the standard models without proper account for the temperature variation of the activation barrier, i.e., the activation entropy. An alternative explanation for the observed weak temperature dependence of the rate[45,51] needs to be sought.

What we found in our previous study[30] and confirmed here is the prevalence of the induction component in X_0. The induction shift becomes more negative with lowering temperature,[30] with the slope consistent with the contraction of the protein matrix. A more negative induction shift means smaller X_0 and a faster reaction rate. This universal feature of the induction interaction of the cofactors with the protein matrix gave a good account of the data by Fleming et al.[45] for the first electron hop, and can potentially explain the temperature effect on similar reactions characterized by small positive X_0 values at room temperature. If this explanation is correct, hydrostatic pressure should affect the rate of primary charge separation in a way qualitatively similar to the temperature variation.

The negative apparent activation enthalpy of primary charge separation is not the only puzzling effect of temperature on the charge-transfer kinetics in bacterial reaction centers. The temperature dependence of the recombination rate is also not quite usual.[10] The recombination rate $k_{30}(T)$ starts with the standard Arrhenius law characterized by a small activation energy of 420
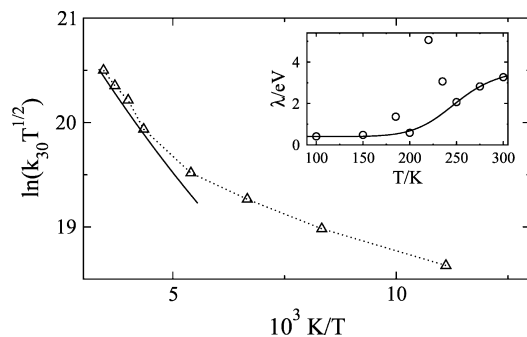
Energetics of Bacterial Photosynthesis

J. Phys. Chem. B, Vol. 113, No. 36, 2009 **12433**

Figure 8. Recombination rate $3 \rightarrow 0$ from experiment[10] (points) and from eq 21 with the energetic parameters from MD simulations, $V_{30} = 2$ cm^{-1}, and $\Delta E_{03}^{gas} = 4.58$ eV. The experimental high-temperature slope is 420 cm^{-1}, while the solid line has a slope of 407 cm^{-1}. The dotted line connects the experimental points. The inset shows the MD results for the reorganization energy λ_{30} with the nonheme iron artificially restrained from leaving the protein matrix. The solid line in the inset is the nonergodic reorganization function fitting the data excluding temperature points 185, 220, and 235 K: $\lambda(T)/\text{eV} = 0.39 + 1.81 \arctan[4108 \times e^{-2000/T}]$. The activation energy of 2000 K arising from an Arrhenius relaxation time is typical for the leading protein/water nuclear mode responsible for solvent reorganization.[26,30]

cm^{-1} and then inflects at about $T_{tr} \simeq 200$ K into a temperature dependence with the activation energy of about 100 cm^{-1} (points in Figure 8). The crossover temperature T_{tr} is consistent with the temperature of dynamical transition in proteins[53] at which collective, anharmonic motions of the protein matrix become active.[54] We have recently shown[26] that the reorganization energy of protein electron transfer drops to the level of half the Stokes shift at T_{tr}.

Our analysis of the recombination transition $3 \rightarrow 0$ at 300 K is consistent with the reported high-temperature portion of the Arrhenius plot of the recombination rate[10] (Figure 8). In particular, the use of the gas-phase energy gap $\Delta E_{03}^{gas} = 4.58$ eV from our analysis with other parameters from simulations yields in the Arrhenius slope of 407 cm^{-1}, very close to the experimental value of 420 cm^{-1}. Our attempts to reproduce the break in the rate slope at lower temperatures by using low-temperature MD simulations were not successful because of the system instability caused by the release of nonheme iron. This problem did not allow us to generate trajectories long enough to produce converged first and second cumulants of the energy gap. Attempts to restrain the motions of nonheme iron inevitably change the energetics and therefore cannot be used for a quantitative analysis. These simulations, however, produced a drop in the reorganization energy similar to the one observed by us for plastocyanin redox protein[26] (inset in Figure 8). This result suggests that the break in the Arrhenius slope can be qualitatively linked to an abrupt drop of the reorganization energy at a temperature close to T_{tr}. We do not however have sufficient data at the moment for a quantitative analysis. Apart from longer trajectories and simulation protocols keeping the nonheme iron from leaving the protein, such an analysis will also require taking into account an inhomogeneous distribution of frozen reaction coordinates realized in an ensemble of reaction centers.

We also briefly comment on the peak of the recombination reorganization energy at T_{tr} (inset in Figure 8). A similar peak in the reorganization energy at exactly the same temperature was observed in our simulations of the half redox reaction of plastocyanin.[26] Since more data were obtained for that system, the peak was found to be narrow, reflecting a weak first-order phase transition of the protein's hydration shell. The reaction

center is much larger than plastocyanin, and a more detailed analysis of this system is presently prohibitively expensive.

Discussion

The application of the standard Marcus theory of electronic transitions to primary bacterial charge separation presents a clear conflict of ideas. While the theory strives to connect the activation barrier of a redox reaction to the electrochemically measurable reaction Gibbs energy, the time scale of primary charge separation makes this connection fundamentally difficult due to a severe breakdown of the system ergodicity, prohibiting the use of the canonical prescription to calculate the reaction energetics.[36] New approaches to connect the activation barrier to observables are required.

The formalism adopted here still follows the traditional route of linking the dynamics to thermodynamics by introducing nonergodic correction factors in front of equilibrium free energies. These corrections, extracted from the equilibrium Stokes shift correlation function provided by MD simulations, allow us to account for short times of the reaction. At the same time, this formalism preserves the linear-response relations (eqs 1 and 2) basic to the Marcus formulation,[55] in clear contrast to the results of numerical simulations.

The analysis of MD trajectories shows a universal breakdown of the connection between the Stokes shift and the reaction coordinate second cumulant (eq 2), thus making the nuclear fluctuations of the bath distinctly non-Gaussian. Whether this is a result of some nonergodic effects not included in the present formalism or the nuclear fluctuations of the protein/water bath are intrinsically non-Gaussian, requires separate studies. We note, however, that a large discrepancy between two routes to the reorganization energy disappears at low temperatures below $T_{tr} \approx 200-230$ K known as the temperature of dynamical transition in proteins.[53,56] The reorganization energy from the width starts to deviate upward from half the Stokes shift at this temperature, rising to its gigantic value at the room temperature.[26] The dynamical transition is commonly associated with the onset of collective anharmonic motions of the protein matrix,[54] which probably modulate the dipolar polarization of the hydration shells[25] and produce a strong electrostatic noise not observed for small and rigid hydrated solutes.

While the microscopic origin of non-Gaussian electrostatic fluctuations inside proteins is an important fundamental question on its own, the question we have pursued here is somewhat different. We want to know if this feature is universal for all electronic transitions in the bacterial reaction center and what does it bring to the reaction kinetics. The answer to the first question is certainly positive, as we show in Table 2. For all five electronic transitions considered here, the reorganization energies obtained from variances (eq 1) are significantly higher than the corresponding values obtained from the Stokes shift (eq 2). The second question, that is, the mechanistic consequences of this observation, is a bit harder to address.

In order to approach the second question, one can start by asking why does nature require a short picosecond time scale for the first electron hop? The answer given by our present simulations is that allowing longer times would make the second hop to H_L proceed with zero driving force and a significant activation barrier, thus effectively halting the entire process. It is simply not possible to not sink the energy of the $P^+ - B_L^-$ state with a 54 D dipole of the charge-separated state if nuclear solvation is allowed. The short time of the reaction freezes nuclear solvation, most effectively water solvation, to a nonergodic reaction free energy amounting to only half of the

TABLE 2: Reaction Free Energies, Reorganization Energies, and Half of the Stokes Shift (All Energies in eV) for Transitions i ↔ f between the Initial, i, and Final, f, States, Where i, f = 0, 1, 2, 3, 4 According to the Reaction Scheme Shown in Figure 2[a]

transition i ↔ f	1 ↔ 2 (L)[b]	1 ↔ 2 (M)[c]	2 ↔ 3	3 ↔ 0	3 ↔ 4[d]
ΔF_{if} (theor.)	−0.19	0.05	−0.06	−0.70	−0.22
ΔG_{if} (exp.)	−0.07[e]	0.1−0.15[f]	−0.18	−1.12	−0.16
λ_{if}	2.36	4.98	2.49	2.24	2.24
λ_{fi}	1.69	1.69	1.98	2.85	3.86
$\Delta X_{if}/2$	0.77	0.54	0.71	0.89	0.96

[a] Calculated here (theor.) and experimental (exp.) reaction free energies are also listed. Unless specified, the experimental reaction free energies are from ref 10. [b] L-branch of the bacterial reaction center. [c] M-branch of the bacterial reaction center. [d] Statistics along the reaction coordinate X_{43} for state 4 were calculated on the MD trajectories obtained for state 1. [e] The only reliably measured reaction gap is $\Delta G_{13} = -0.25$ eV, which is exactly equal to the gap obtained from the theoretical calculations presented here, $\Delta F_{12} + \Delta F_{23} = -0.25$ eV. [f] From ref 35.

equilibrium value. At the same time, a significant solvation energy of the charge-separated state is used to dynamically achieve the resonance condition for the second electron hop. The nuclear subsystem relaxes on the time scale of the first electronic transition toward equilibrium with the charge-separated state just enough to allow a zero barrier transition for the second hop (Figure 4). The equilibrium reaction free energy of about −0.06 eV is thus not required for the reaction to occur and is achieved by a subsequent nuclear relaxation to equilibrium. This calculation thus reveals a remarkable novel mechanism of achieving fast unidirectional electron transfer, not through the adjustment of a negative reaction free energy but through the adjustment of the time scale such that the system always has a chance to cross the state of activationless transition in the course of nuclear relaxation following the first electron hop.

If bacterial charge transfer were following the traditional prescription for activationless transitions within the Marcus model, the entire energy of the incoming photon $h\nu = 1.37$ eV would have been spent on just two first electron hops, $\Delta G_{13} = -(\Delta X_{12} + \Delta X_{23})/2 = -1.48$ eV (Table 2). What the broad distribution of the energy gaps, with a large reorganization energy, provides is a much lower drop in the reaction free energy than is traditionally anticipated. We discuss this point below in application to the principles of operation of artificial photosynthesis. We just note here that flat free energy surfaces found here provide much less sensitivity of the kinetics to the variations in the driving force, and thus, more robust design is achieved. At the same time, the puzzling increase of the primary charge separation rate with lowering temperature[45] has received a natural explanation in terms of the temperature dependence of the induction component dominating the average donor−acceptor energy gap. For slower reactions, as is the case of the 3 → 0 recombination, this feature is supplemented by a break in the Arrhenius slope originating from the decay of the reorganization energy when collective protein motions freeze in. This result, reported here for the bacterial reaction center protein, is probably a general property of hydrated proteins[26] that might be invoked to explain several reports[10,57,58] of slope breaks in Arrhenius plots of photosynthetic reaction rates.

Lessons for Artificial Photosynthesis

We have studied here five electronic transitions belonging to the kinetic scheme of bacterial primary charge separation
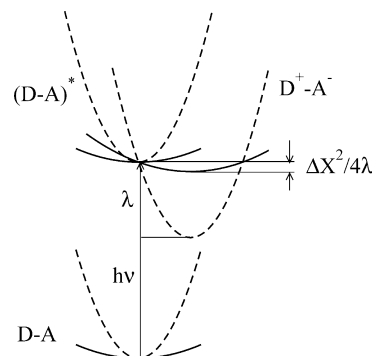

Figure 9. Energetic scheme of molecular photosynthesis: donor−acceptor complex D−A, its photoexcited state (D−A)*, and the charge-separated state D$^+$−A$^-$. Activationless charge separation, following photoexcitation with the visible quantum $h\nu$, results in the loss of free energy λ in the standard Marcus model and in the loss $\Delta X^2/(4\lambda)$ when the nuclear fluctuations become non-Gaussian and eq 2 does not apply anymore. This change of energetics will result in $(2\lambda/\Delta X)^2$ electron hops in the new description per one electron hop in the standard picture. The dashed lines represent the standard Marcus parabolas, and the solid lines are parabolic approximates of globally non-parabolic surfaces close to their minima.

(Figure 2). Their kinetics and energetics were found to be remarkably consistent with the existing experimental database. We have arrived at this agreement despite the reorganization parameters, reorganization energies in particular, significantly different from the traditionally accepted values.[5] In fact, many mechanistic aspects of charge-transfer transitions elucidated here present a significant departure from the assumptions traditionally incorporated into the calculation of electron-transfer rates in nonprotein donor−acceptor complexes. One therefore wonders if any of these new principles of operation uncovered for protein media can be applied to artificial photosynthetic systems. We will briefly dwell on this question, focusing in particular on the energetic efficiency of artificial photosynthesis.

Both natural and synthetic molecular photosynthetic systems follow the same basic energetic scheme in which the photoexcitation of the donor−acceptor complex leads to a charge-separated state ((D−A)* → D$^+$−A$^-$ in Figure 9). In order to defeat the wasteful recombination process, bacterial complexes employ successive activationless hops spatially separating the donor and acceptor moieties and diminishing their electronic overlap. According to the standard Marcus picture, each of these activationless hops requires losing the reorganization energy λ to the phonons of the thermal bath (dashed curves in Figure 9). On the contrary, when the link between the parabolas' curvature and the Stokes shift breaks down, the energy lost in each hop is $\Delta X^2/(4\lambda)$. Therefore, when the condition $\Delta X < 2\lambda$ found for proteins is realized, the parameter

$$\chi_{NG} = (2\lambda/\Delta X)^2 \qquad (22)$$

can be viewed as a measure of energetic efficiency enhancement by the non-Gaussian statistics of the energy gap fluctuations. It defines the number of electron hops allowed in the non-Gaussian picture per one electron hop in the standard Gaussian picture. With the reorganization parameters presented in Table 2, $\chi_{NG} \simeq 10$ and this new paradigm predict an order-of-magnitude increase in the energetic efficiency of solar energy conversion. As is seen in Figure 10, the value of χ_{NG} is fairly consistent for all electronic transitions found in the L-branch of the reaction center.

Energetics of Bacterial Photosynthesis

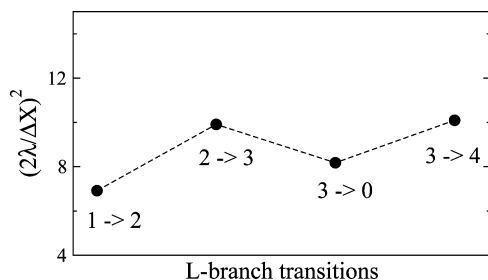*J. Phys. Chem. B, Vol. 113, No. 36, 2009* **12435**

Figure 10. Number of electron hops in the non-Gaussian picture per one electron hop in the Gaussian paradigm. Approximately an order of magnitude increase in the energetic efficiency of biological electron transport chains is achieved for all electronic transitions in the L-branch of the reaction center. Mean reorganization energies $\lambda = (\lambda_{if} + \lambda_{fi})/2$ from Table 2 were used to produce the points.

The protein/water interface shows the existence of two distinctly different time scales in its polar response. The cofactors "see" the thermal bath as nonpolar at the picosecond time scale, but it becomes very polar at the nanosecond time scale (e.g., $\lambda_{12} = 0.35$ eV at 4 ps vs $\lambda_{12} = 2.36$ eV at 10 ns). Each of these polarity regimes operates correspondingly for charge separation and charge recombination, producing a "switching mechanism" in the environmental control of the reaction rate. It might therefore be expected that electronic transitions either on the scale of a few picoseconds or on a much longer scale of subnanoseconds and longer should be observed in natural systems. One also wonders if a similar switching mechanism can be realized in synthetic systems as a means to diminish wasteful recombination processes.

We also need to emphasize that global non-parabolic free energy surfaces of electron transfer[28] are required for a complete description of the non-Gaussian statistics of the energy gap fluctuations observed here. Which functionality will reproduce the numerical simulations is currently unknown. Presently, the absence of reliable analytical models extending electron-transfer theory beyond the Gaussian picture is the main obstacle to analyzing the increasing database produced by numerical simulations, as has been indeed the case in this study. Further studies in this direction are required, in particular for protein electron transfer, to address the problem of the overall energetic efficiency of biological machines. All of them operate with the energy input of the order of $1-1.5$ eV provided by either the redox potential of food supply or the light photon.[59] They all rely on a chain of electron hops which would be hard to realize if the loss of energy of the order of $\Delta X/2$ (Table 2) were required at each electronic transition.

Appendix: Parametrization of the Polarizable Special Pair.

The parameters of the two-state model of the photoexcited special pair (Figure 11) where obtained from fitting to available experimental data. Stark spectroscopy data by Lockhart and Boxer[60] recorded at $T = 77$ K suggest that the change in the dipole moment upon photoexcitation is larger by $f_c\Delta\mu = 7$ D in the bacteriochlorophyll dimer than in an isolated bacterio-
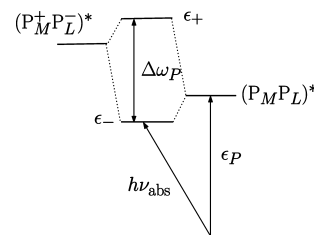

Figure 11. Energy diagram of the electronic states of the photoexcited special pair. The absorption frequency of the special pair $h\nu_{abs}$ is red-shifted relative to the unperturbed energy gap ε_P by the excitonic coupling J between the neutral and ionized states of the special pair. The energy gap between the eigenvalues of the two-state Hamiltonian is $\Delta\omega_P$.

chlorophyll ($f_c \simeq 1.2$ is the correction factor for the cavity field). If the change in the dipole moment is connected to the mixing between the fully covalent $(P_M-P_L)^*$ and fully ionized $(P_M{}^+-P_L{}^-)^*$ states of the photoexcited special pair, then it becomes $\Delta\mu = n_{CT}\Delta\mu_{CT}$, where $\Delta\mu_{CT}$ and n_{CT} are, respectively, the dipole moment and the population of the ionized state. From the two-state Hamiltonian, the latter is given as

$$n_{CT} = \frac{1}{2} - \frac{\Delta\varepsilon}{2\Delta\omega_P} \tag{23}$$

Here, $\Delta\varepsilon$ is the difference between diabatic energies of the ionized and neutral states, and $\Delta\omega_P$ is the adiabatic energy gap between the eigenvalues of the two-state Hamiltonian, ε_+ and ε_- in Figure 11. It is given by the relation

$$\Delta\omega_P = (\Delta\varepsilon^2 + 4J^2)^{1/2} \tag{24}$$

The diabatic energy gap $\Delta\varepsilon$ in eqs 23 and 24 is a sum of the gas-phase component $\Delta\varepsilon^{gas}$, the induction shift $\Delta\varepsilon^{ind}$, and the Coulomb shift $\Delta\varepsilon^C$:

$$\Delta\varepsilon = \Delta\varepsilon^{gas} + \Delta\varepsilon^{ind} + \Delta\varepsilon^C \tag{25}$$

Further, J in eq 24 is the electronic coupling element between the lower excitonic state of P^* and the charge-transfer state.[38] When two bacteriochlorophyll radicals $P_M{}^+$ and $P_L{}^-$ are placed at the crystallographic positions, the dipole moment is $\Delta\mu_{CT} = 40.2$ D, which gives the population of the ionized state $n_{CT} = 0.143$ at 77 K.

Both the induction and Coulomb components of the energy gap $\Delta\varepsilon$ in eq 25 depend on the distribution of charge between the neutral and ionized states of the special pair. Since the population of the ionized state (eq 23) is itself affected by the energy gap, a self-consistent procedure needs to be applied to parametrize the gas-phase component of the energy gap $\Delta\varepsilon^{gas}$. The electronic coupling J needs to be determined first, and that was done by adopting the adiabatic energy gap of $\Delta\omega_P = 2800$ cm^{-1} from the model vibronic Hamiltonian of Lathrop and Friesner[38] parametrized by fitting the model to a number of low-temperature experimental spectra. Combined with the low-temperature population of the ionized state $n_{CT} = 0.143$ from Lockhart and Boxer,[60] this calculation yields $J = 979$ cm^{-1} and $\Delta\varepsilon = 1998$ cm^{-1}. We next run a series of short, 100 ps long, simulations in a NPT ensemble at 77 K, with the gas-phase component $\Delta\varepsilon^{gas}$ in eq 25 held fixed in each simulation. The average population of the ionized state was then plotted against
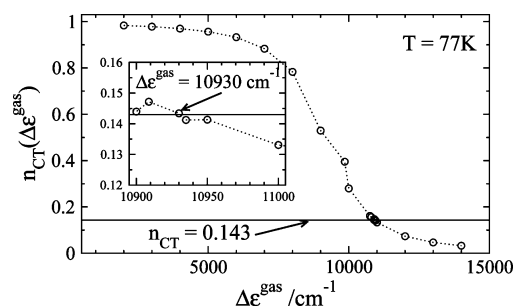
Figure 12. Population of the ionized state of the photoexcited special pair as a function of the gas-phase energy gap of the two-state Hamiltonian. The points are from 100 ps MD simulations at 77 K; the solid line denotes the experimental population extracted from Stark spectra recorded at $T = 77$ K.[60] The inset shows a magnified portion of the plot at the intersection of the simulated and experimental lines.
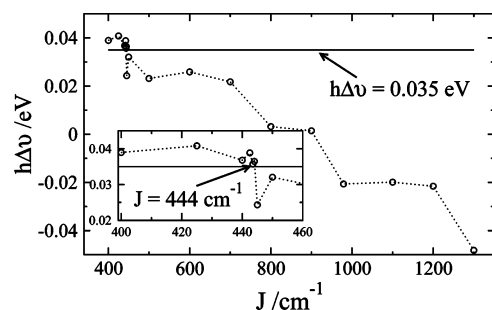

Figure 13. Temperature shift of the absorption band of the special pair between 77 and 300 K, $h\Delta\nu = h\nu(300\ \text{K}) - h\nu(77\ \text{K})$, as a function of the electronic coupling J. The experimental value[51] of the shift, 0.035 eV, is shown by the solid line. Points represent 100 ps simulations at 300 K run at different values of J. The inset magnifies the part of the plot where the intersection between the simulation and experimental lines is achieved.

$\Delta\varepsilon^{\text{gas}}$ (Figure 12) to give us $\Delta\varepsilon^{\text{gas}} = 10930\ \text{cm}^{-1}$ that reproduces the experimental Stark value $n_{\text{CT}} = 0.143$.

The gas-phase energy gap obtained from calibration at 77 K can be directly used in simulations at room temperature given that the induction and Coulomb components in the energy gap are calculated at instantaneous nuclear configurations of the system, with the corresponding adjustment of the population according to eq 23. The off-diagonal coupling may however depend on temperature[61] due to low-frequency vibrations of the special dimer,[62] and the value obtained at 77 K is not reliable. In order to address this effect, one can adjust the model to the experimentally established temperature shift of the primary absorption band, $h\Delta\nu = h\nu(300\ \text{K}) - h\nu(77\ \text{K}) = 0.035$ eV.[51,63]

The observable primary absorption frequency is red-shifted from the energy ε_{P} by the coupling between the neutral and ionized states (Figure 11). The difference between ε_{P} and the lower adiabatic energy ε_- is $\Delta e = \Delta\omega_{\text{P}}/2 - \Delta\varepsilon/2$. If the temperature variation of the absorption energy is caused by the change in the electronic overlap between two states of the special pair, one can adjust J to the experimental thermochromic blue shift $h\Delta\nu = \Delta e(300\ \text{K}) - \Delta e(77\ \text{K})$. To this end, we run a series of short 100 ps simulations at 300 K with varying matrix element J. The experimental shift of the absorption band can be achieved by decreasing J from its 77 K values $J = 979\ \text{cm}^{-1}$ to $J = 444\ \text{cm}^{-1}$ (Figure 13). This latter value was adopted for our longer production runs at 300 K.

Supporting Information Available: Description of the simulation protocol. This material is available free of charge via the Internet at http://pubs.acs.org.

References and Notes

(1) Hoff, A. J.; Deisenhofer, J. *Phys. Rep.* **1997**, *287*, 1.
(2) Zinth, W.; Wachtveitl, J. *ChemPhysChem* **2005**, *6*, 871.
(3) Marcus, R. A. *J. Chem. Phys.* **1956**, *24*, 966.
(4) Chen, P.; Meyer, T. J. *Chem. Rev.* **1998**, *98*, 1439.
(5) Bixon, M.; Jortner, J. *Adv. Chem. Phys.* **1999**, *106*, 35.
(6) Sumi, H.; Kakitani, T. *J. Phys. Chem. B* **2001**, *105*, 9603.
(7) Jia, Y.; DiMagno, T. J.; Chan, C.-K.; Wang, Z.; Du, M.; Hanson, D. K.; Schiffer, M.; Norris, J. R.; Fleming, G. R. *J. Phys. Chem.* **1993**, *97*, 13180.
(8) Nagarajan, V.; Parson, W. W.; Davis, D.; Schenck, C. C. *Biochemistry* **1993**, *32*, 12324.
(9) Bixon, M.; Jortner, J.; Michel-Beyerle, M. E. *Chem. Phys.* **1995**, *197*, 389.
(10) Volk, M.; Aumeier, G.; Langenbacher, T.; Feick, R.; Ogrodnik, A.; Michel-Beyerle, M.-E. *J. Phys. Chem. B* **1998**, *102*, 735.
(11) Wang, H.; Lin, S.; Allen, J. P.; Williams, J. C.; Blankert, S.; Laser, C.; Woodbury, N. W. *Science* **2007**, *316*, 747.
(12) Treutlein, H.; Schulten, K.; Brünger, A. T.; Karplus, M.; Deisenhofer, J.; Michel, H. *Proc. Natl. Acad. Sci.* **1992**, *89*, 75.
(13) Marchi, M.; Gehlen, J. N.; Chandler, D.; Newton, M. *J. Am. Chem. Soc.* **1993**, *115*, 4178.
(14) Alden, R. G.; Parson, W. W.; Chu, Z. T.; Warshel, A. *J. Am. Chem. Soc.* **1995**, *117*, 12284.
(15) Parson, W. W.; Chu, Z. T.; Warshel, A. *Biophys. J.* **1998**, *74*, 182.
(16) Ceccarelli, M.; Marchi, M. *J. Phys. Chem. B* **2003**, *107*, 5630.
(17) Ceccarelli, M.; Marchi, M. *J. Phys. Chem. B* **2003**, *107*, 1423.
(18) Sterpone, F.; Ceccarelli, M.; Marchi, M. *J. Phys. Chem. B* **2003**, *107*, 11208.
(19) Hwang, J.-K.; Warshel, A. *J. Am. Chem. Soc.* **1987**, *109*, 715.
(20) Kuharski, R. A.; Bader, J. S.; Chandler, D.; Sprik, M.; Klein, M. L.; Impey, R. W. *J. Chem. Phys.* **1988**, *89*, 3248.
(21) Blumberger, J.; Sprik, M. *Theor. Chem. Acc.* **2006**, *115*, 113.
(22) Kriegl, J. M.; Nienhaus, G. U. *Proc. Natl. Acad. Sci. U.S.A.* **2004**, *101*, 123.
(23) Li, T.; Hassanali, A.; Kao, Y.-T.; Zhong, D.; Singer, S. *J. Am. Chem. Soc.* **2007**, *129*, 3376.
(24) Khodadadi, S.; Pawlus, S.; Sokolov, A. P. *J. Phys. Chem. B* **2008**, *112*, 14273.
(25) LeBard, D. N.; Matyushov, D. V. *J. Phys. Chem. B* **2008**, *112*, 5218.
(26) LeBard, D. N.; Matyushov, D. V. *Phys. Rev. E* **2008**, *78*, 061901.
(27) Ghorai, P. K.; Matyushov, D. V. *J. Chem. Phys.* **2006**, *124*, 144510.
(28) Matyushov, D. V. *Acc. Chem. Res.* **2007**, *40*, 294.
(29) Ito, N.; Duvvuri, K.; Matyushov, D. V.; Richert, R. *J. Chem. Phys.* **2006**, *125*, 024504.
(30) LeBard, D. N.; Kapko, V.; Matyushov, D. V. *J. Phys. Chem. B* **2008**, *112*, 10322.
(31) Tan, M.-L.; Dolan, E.; Ichiye, T. *J. Phys. Chem. B* **2004**, *108*, 20435.
(32) Heller, B. A.; Holten, D.; Kirmaier, C. *Science* **1995**, *269*, 940.
(33) Zhang, L. Y.; Friesner, R. A. *Proc. Natl. Acad. Sci. U.S.A.* **1998**, *95*, 13603.
(34) Chuang, J. I.; Boxer, S. G.; Holten, D.; Kirmaier, C. *Biochemistry* **2006**, *45*, 3845.
(35) Chuang, J. I.; Boxer, S. G.; Holten, D.; Kirmaier, C. *J. Phys. Chem. B* **2008**, *112*, 5487.
(36) Matyushov, D. V. *J. Chem. Phys.* **2009**, *130*, 164522.
(37) Middendorf, T. R.; Mazzola, L. T.; Lao, K. Q.; Steffen, M. A.; Boxer, S. G. *Biochim. Biophys. Acta* **1993**, *1143*, 223.
(38) Lathrop, E. J. P.; Friesner, R. A. *J. Phys. Chem.* **1994**, *98*, 3056.
(39) Johnson, E. T.; Müh, F.; Nabedryk, E.; Williams, J. C.; Allen, J. P.; Lubitz, W.; Breton, J.; Parson, W. W. *J. Phys. Chem. B* **2002**, *106*, 11859.
(40) Duan, Y.; Wu, C.; Chowdhury, S.; Lee, M. C.; Xiong, G.; Zhang, W.; Yang, R.; Cieplak, P.; Luo, R.; Lee, T.; Caldwell, J.; Wang, J.; Kollman, P. *J. Comput. Chem.* **2003**, *24*, 1999.
(41) Jorgensen, W. L.; Chandrasekhar, J.; Madura, J. D.; Impey, R. W.; Klein, M. L. *J. Chem. Phys.* **1983**, *79*, 926.
(42) van Duijnen, P.; Swart, M. *J. Phys. Chem. A* **1998**, *102*, 2399.
(43) Caldwell, J. W.; Kollman, P. A. *J. Phys. Chem.* **1995**, *99*, 6208.
(44) Matyushov, D. V.; Voth, G. A. *J. Chem. Phys.* **2000**, *113*, 5413.
(45) Fleming, G. R.; Martin, J. L.; Breton, J. *Nature* **1988**, *333*, 190.
(46) Takiff, L.; Boxer, S. G. *J. Am. Chem. Soc.* **1988**, *110*, 4425.
(47) Wakeham, M. C.; Jones, M. R. *Biochem. Soc. Trans.* **2005**, *33*, 851.
(48) Steffen, M. A.; Lao, K.; Boxer, S. G. *Science* **1994**, *264*, 810.
(49) Frolov, D.; Gall, A.; Lutz, M.; Robert, B. *J. Phys. Chem. A* **2002**, *106*, 3605.
(50) Alden, R. G.; Parson, W. W.; Chu, Z. T.; Warshel, A. *J. Phys. Chem.* **1996**, *100*, 16761.

Energetics of Bacterial Photosynthesis

J. Phys. Chem. B, Vol. 113, No. 36, 2009 **12437**

(51) Kirmaier, C.; Holten, D. In *Photosynthetic Bacterial Reaction Center: Structure and Dynamics*; Breton, J., Vermégio, A., Eds.; Plenum: New York, 1988; Vol. 149, pp 219−228.

(52) Haffa, A. L. M.; Lin, S.; Katilius, E.; Williams, J. C.; Taguchi, A. K. W.; Allen, J. P.; Woodbury, N. W. *J. Phys. Chem. B* **2002**, *106*, 7376.

(53) Parak, F. G. *Rep. Prog. Phys.* **2003**, *66*, 103.

(54) Fenimore, P. W.; Frauenfelder, H.; McMahon, B. H.; Young, R. D. *Proc. Natl. Acad. Sci.* **2004**, *101*, 14408.

(55) Marcus, R. A.; Sutin, N. *Biochim. Biophys. Acta* **1985**, *811*, 265.

(56) Caliskan, G.; Briber, R.; Thirumalai, D.; Garcia-Sakai, V.; Woodson, S.; Sokolov, A. *J. Am. Chem. Soc.* **2006**, *128*, 32.

(57) Ortega, J. M.; Mathis, P.; Williams, J. C.; Allen, J. P. *Biochemistry* **1996**, *35*, 3354.

(58) Xu, Q.; Gunner, M. R. *J. Phys. Chem. B* **2000**, *104*, 8035.

(59) Nicholls, D. G.; Ferguson, S. J. *Bioenergetics 2*; Academic Press: London, 1992.

(60) Lockhart, D. J.; Boxer, S. G. *Proc. Natl. Acad. Sci. U.S.A.* **1988**, *85*, 107.

(61) Chang, C. H.; Hayashi, M.; Liang, K. K.; Chang, R.; Lin, S. H. *J. Phys. Chem. B* **2001**, *105*, 1216.

(62) Vos, M. H.; Martin, J.-L. *Biochim. Biophys. Acta* **1999**, *1411*, 1.

(63) Huber, H.; Meyer, M.; Scheer, H.; Zinth, W.; Wachtveil, J. *Photosynth. Res.* **1998**, *55*, 153.